JOURNAL OF GEOPHYSICAL RESEARCH, VOL. 105, NO. D2, PAGES 2029–2043, JANUARY 27, 2000

Regional aerosol distribution and its long-range transport over the Indian Ocean

K. Rajeev, V. Ramanathan, and J. Meywerk

Center for Clouds, Chemistry and Climate, Scripps Institution of Oceanography, La Jolla, California

Abstract. Aerosol chemical, microphysical, and optical data collected from an island station and a ship during the first field phase of the Indian Ocean Experiment provided a unique opportunity to develop models for retrieving aerosol optical depth from the advanced very high resolution radiometer (AVHRR) onboard NOAA14 during January–March 1998. Columnar aerosol optical depth (AOD) over Arabian Sea, Bay of Bengal, and Indian Ocean was derived for the 630 nm wavelength from the radiance in channel 1 (580–680 nm) of AVHRR. The satellite retrieval model for AOD accounts for several aerosol species (sulfates, nitrates, sea salt, soot, dust, and organics), the in situ measured value of single scattering albedo, and the wind speed dependence of sea surface albedo. Satellite-retrieved AOD is in good agreement with surface measurements of AOD taken from the Indian Ocean island of Kaashidhoo (4.96°N, 73.46°E) in the Maldives and from the R/V *Sagar Kanya* cruising between 20°N and 20°S. The success of our model is most likely due to the use of observed single scattering albedo, the use of phase function derived from in situ data, and the limitation of the analysis to the antisolar side of the satellite scan. However, the model relies on atmospheric column data and surface measurements, which need future verification with in situ aircraft data. Regional maps reveal that the entire northern Indian Ocean has large 0.15 AOD with monthly mean values exceeding 0.2 for latitudes north of ~5°N, for all 3 months. AOD increases northward, reaching values as high as 0.35 toward the coast in the Bay of Bengal and the Arabian Sea. The non-sea-salt component of AOD is inferred to be more than 3 times that of the estimated wind-dependent sea salt component. In the western Indian Ocean and Arabian Sea the high concentration of non-sea-salt aerosols are due to transport from the Indian subcontinent and Arabia. The eastern Indian Ocean is influenced by the transport from the Indian subcontinent and southeast Asia, particularly from Indonesia. The 1998 El Niño-related forest fires from Indonesia resulted in high AOD values (0.25–0.35) in the eastern equatorial Indian Ocean. Minimum AOD is observed between the equator and 10°S, which is the location of the Intertropical Convergence Zone (ITCZ) during the observation period. AOD is generally found to increase to the south of ITCZ and reach a maximum around 20°S.

1. Introduction

Unlike greenhouse gases, tropospheric aerosols have short lifetimes (about few weeks or less), and therefore their spatial distribution is highly inhomogeneous and strongly correlated with their sources. Satellite-based remote sensing of aerosols remains the most convenient method to study spatial and temporal distributions of aerosol optical depth on regional and global scale. However, satellite retrieval of aerosol optical depth requires a priori information about the scattering and absorbing properties of the aerosols.

Upwelling radiances at the top of atmosphere observed by satellite sensors having smaller spectral bandwidths could be inverted to determine aerosol optical depth (AOD) if the aerosol scattering phase function and the complex refractive index are known. Examples of such inversions include the advanced very high resolution radiometer (AVHRR) [*Stowe et al*., 1997], Sea-viewing Wide Field-of-view Sensor (SeaWiFS) [*Gordon and Wang*, 1994], and Moderate-Resolution Imaging Spectrometer (MODIS) [*Kaufman et al*., 1997] among others. Accuracy of the AOD retrieved from satellite data, however, depends on aerosol single scattering albedo [*Mishchenko and Travis*, 1997], phase function, and surface reflectivity [*Stowe et al*., 1997, *Kaufman et al*., 1997] assumed in the inversion.

Here we have studied the spatial distribution of aerosol optical depth over the tropical Indian Ocean, Arabian Sea, and Bay of Bengal based on AOD retrieved from the AVHRR visible channel (630 ± 50 nm) radiances during January 1 to March 31, 1998. The aerosol scattering phase function and single scattering albedo used in the retrieval were obtained by integrating surface aerosol chemical and microphysical data with observed columnar aerosol optical depths and a comprehensive aerosol model [*Satheesh et al*., 1999]. The data were collected during February to March 1998 as part of the first field phase (FFP) of the Indian Ocean Experiment (INDOEX) [*Ramanathan et al*., 1995, 1996]. INDOEX is aimed at studying the long-range transport of trace species and aerosols from urban regions and assessing their direct and indirect radiative forcing. The Indian Ocean is selected as the study area for the following reasons:

1. The northeast Indian monsoon region bordered to the

Paper number 1999JD900414.
0148-0227/00/1999JD900414$09.00

Table 1. Individual Components of the Aerosol Model Used in This Study and the Normalized Number Density N_i, Mode Radius r_{mi}, and Width σ_{mi} of the Lognormal Aerosol Size Distribution Describing Each of Them at RH = 75%

Component	N_i	r_{mi}, μm	σ_{mi}
Sulfate, nitrate, ammonia, and organics	0.20210	0.0295	2.24
Sea salt (accumulation)	1.19664×10^{-4}	0.3970	2.03
Sea salt (coarse)	1.10637×10^{-6}	3.3300	2.03
Mineral (Transport)	1.83485×10^{-5}	0.5000	2.20
Soot	0.79776	0.0118	2.00

RH is relative humidity.

south by the vast Indian Ocean and to the north by the densely populated and rapidly developing Indian subcontinent is a unique laboratory to study the extent to which continental aerosols are transported over relatively clean ocean areas thousands of kilometers away from the sources. Wind is northerly to northeasterly from the continents in the Northern Hemisphere at the surface and the lower tropospheric levels during January–March and has the potential to transport aerosols from polluted continental areas deep into the otherwise pristine ocean areas. The ITCZ is located close to or south of the equator during most of this period. This gives a unique opportunity to study the extent of transport of continental aerosols [*Ramanathan et al*., 1995, 1996].

2. Despite this unique feature, only very few measurements of aerosol characteristics had been carried out over the Indian Ocean [*Prodi et al*., 1983; *Savoie et al*., 1987; *Chester et al*., 1991]. More recently, measurements of aerosol characteristics were made over the Indian Ocean as part of INDOEX [*Jayaraman et al*., 1997; *Krishna Moorthy et al*., 1997; *Rhoads et al*., 1997; *Krishnamurti et al*., 1998]. Several of these studies have shown the transport of continental aerosols into the Arabian Sea and the Indian Ocean.

Measurements of aerosol physical and chemical properties were carried out during the INDOEX FFP. They include ground-based aerosol measurements at Kaashidhoo Island (4.96°N, 73.46°E) in Maldives during the continuous observation period between February 22 and March 31, 1998, and measurements onboard R/V *Sagar Kanya* during its cruise period between February 18 and March 28, 1998. Measurements of physical, chemical, and optical properties of aerosols made at Kaashidhoo were used to develop a model of aerosol size distribution and single scattering albedo, which is described by *Satheesh et al*. [1999]. We have used this model to retrieve aerosol optical depth from AVHRR data. The aerosol retrieval is performed on the basis of look-up tables of top-of-atmosphere radiance generated using the discrete ordinate radiative transfer method, which takes into account the multiple scattering by aerosols and molecules [*Stamnes et al*., 1988]. Retrieval of aerosol optical depth is carried out only over ocean, where the surface reflectance can be calculated with reasonable accuracy. Variations in ocean reflectance due to wind speed are taken into account by considering daily surface winds from the National Centers for Environmental Prediction (NCEP)/National Center for Atmospheric Research (NCAR) reanalysis [*Kalnay et al*., 1996] during the same period of observation. We have also studied the effect of varying aerosol phase function, single scattering albedo, and wind speed on the retrieved AOD.

Section 2 describes the algorithm for aerosol retrieval and the method of analysis of AVHRR data. Validation of the retrieved AOD by comparing with in situ measurements and the effect of single scattering albedo and wind speed on the retrieved AOD are discussed in section 3. Spatial distribution of AOD during January, February, and March are described in section 4. The role of the prevailing atmospheric circulation in transporting aerosols into the ocean and the source regions for different ocean areas are discussed in section 5.

2. Algorithm, Data, and Method of Analysis

2.1. Algorithm

Over ocean, reflectance observed by the satellite sensor comprises contributions from the radiation scattered by aerosols and molecules in the atmosphere, the direct and diffuse solar radiation reflected from the surface into the direction of the sensor, and the water leaving radiance due to scattering by particles in the ocean. The contribution due to water leaving radiance at the wavelengths of our interest is very small and may be neglected [*Tanre et al*., 1992]. Ocean reflection arises from fresnel reflection by the waves called glitter and the reflection by white caps.

Radiance due to scattering by aerosols and molecules depends on their respective concentrations, the scattering phase function ($P(\theta)$), and the single scattering albedo (ω). In this study we have used the aerosol scattering phase function and single scattering albedo based on the aerosol model developed for the Indian Ocean during the same observation period [*Satheesh et al*., 1999]. The aerosol model is based on the spectral column aerosol optical depth measurements using the CIMEL radiometer [*Holben et al*., 1998] and the size-resolved aerosol chemical measurements at the surface, which were integrated to the comprehensive aerosol model of *Hess et al*. [1998]. This aerosol model contains seven aerosol types, namely, sea salt, sulfate, nitrate, organics, ammonia, dust, and soot. Each of these components is assumed to have lognormal size distribution. The mode radius r_m and width σ_m of the distribution and the normalized number concentration N of each of these components are given in Table 1. In the present study we assume that this aerosol model represents the vertical column. In this aerosol model the observed mean single scattering albedo at surface is 0.90 and corresponds to a mean relative humidity of 78% observed during the period. However, the mean relative humidity varies with height, which results in the height variation of single scattering albedo [*Hess et al*., 1998]. For the above described aerosol model the values of ω with relative humidity (RH) are 0.90 for RH = 78%, 0.874 for RH = 70%, 0.861 for RH = 60%, 0.850 for RH = 50%, and 0.752 for RH = 35%.

In the present study we have taken the average altitude profile of RH based on the balloon sonde data during the observation period as given by *Satheesh et al*. [1999] and used the corresponding value of aerosol single scattering albedo. The altitude profile of RH has a mean value of 78% in the

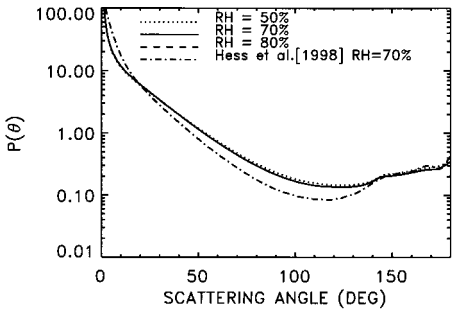

Figure 1. Scattering phase function of the aerosol model used at relative humidities (RH) of 50, 70, and 80%. Aerosol scattering phase function of the tropical marine aerosol model by *Hess et al*. [1998] is also shown for comparison.

mixing region (up to 1 km) and decreases above 1 km to have a mean value of 62% between 1 and 2 km. Above 2 km, RH shows only little variation and has a mean value of 35%. Figure 1 shows the aerosol scattering phase function used to retrieve AOD from satellite radiance in channel 1 (630 ± 50 nm) for three values of RH: 50, 70, and 80%. Also shown in Figure 1 is the phase function corresponding to the marine aerosol model by *Hess et al*. [1998] for comparison. Variation of phase function in the relative humidity range of 50–80% is negligible. Further, scattering phase functions of the observed aerosol model and the marine model of *Hess et al*. [1998] are very close in the scattering angle of 150°–180°, which is the range of scattering angles of backscattered radiation (reaching the satellite sensor) used in this study.

Fresnel reflection of the direct and diffuse solar radiation at the ocean surface varies with wind speed and is calculated for rough ocean on the basis of the model proposed by *Cox and Munk* [1954]. This model gives probability distribution of surface slopes as a function of wind speed and direction. Magnitude of the surface reflectance and its variation with wind speed are maximum at the solar side of satellite scan, and the error in retrieved AOD will be larger in this region because of any uncertainty in the actual wind speed. We avoid data at the solar side of the satellite scan and use data from the antisolar side of satellite scan with a viewing angle >40° away from specularly reflected ray. In this antisolar side of satellite scan region, variability in sea surface reflectance is mainly caused by wind speed variation, and the variability is higher at higher wind speed. The effect of wind direction on surface reflectance is rather small. We have considered the effect of wind speed on ocean reflectance and used a constant northeasterly wind direction. Assuming constant wind direction does not produce any significant error in the retrieved AOD since the effect is significant only at very high wind speeds. Such very high wind speeds are usually observed in association with a weather system during which cloud cover does not allow aerosol retrieval based on satellite radiances.

Increase in wind speed also causes increase in ocean albedo by increasing the percentage of sea covered by foam (white caps). We include this effect on the basis of the model produced by *Koepke* [1984]. Reflectance due to white caps is, however, significant only at wind speeds $>\sim 10$ m s^{-1}.

2.2. The Look-Up Table

Look-up tables of satellite altitude radiances as a function of solar zenith angle and satellite viewing angle are generated using the discrete ordinate radiative transfer method for a plane parallel atmosphere [*Stamnes et al*., 1988] with 32 vertical layers. This method accounts for the multiple scattering by aerosols and molecules and absorption due to aerosols, water vapor, and ozone.

The look-up table of the radiance is generated at 5° intervals of solar and satellite zenith angles and 10° intervals of relative azimuth between the Sun and satellite for different columnar aerosol optical depths at an interval of 0.1. The radiances are simulated for three wind speeds: 4, 8, and 12 m s^{-1}. The simulated radiances correspond to two cases: (1) the absorbing aerosol model (with $\omega = 0.90$ at the surface) described in section 2.1 and (2) a nonabsorbing case ($\omega = 1.0$) corresponding to the same phase function used in the previous case. Altitude variation of RH and the corresponding variation of ω for the absorbing aerosol model are described in section 2.1. Vertical profiles of pressure, temperature, molecular density, and ozone for the tropical atmosphere are based on the model by *McClatchey et al*. [1972]. Aerosols are assumed to be well mixed in the boundary layer (up to 1 km), and the aerosol number density decreases exponentially above 1 km with a scale height of 0.8 km, which is inferred from the lidar images during the observation period [*Satheesh et al*., 1999]. Response functions of NOAA14 AVHRR visible and near-IR channels are considered by integrating monochromatic radiances simulated at 14 spectral bands in the wavelength range 550–1100 nm. Absorption of radiation by water vapor and ozone are accounted for by using the correlated k distribution technique [*Kratz*, 1995; *Chou and Lee*, 1996].

2.3. Data and Method of Analysis

We have used the NOAA14 AVHRR global area coverage (GAC) data of the 1430 LT satellite pass in the latitude range 25°S to 25°N and the longitude range 40°–100°E during the period January 1, 1998, to March 31, 1998. AVHRR has five wavelength bands of observation, namely, visible (channel 1: ≈580–680 nm), near infrared (channel 2: ≈720–1100 nm), and infrared (channel 3: ≈3.5–4.0 μm; channel 4: ≈10.5–11.5 μm; and channel 5: ≈11.5–12.5 μm). Channel 1 radiances are used for retrieving AOD over the ocean areas. Brightness temperature derived from channels 4 and 5, along with radiance from channels 1 and 2, are used for cloud detection. All three satellite passes per day available in this region are used. Pixel resolution of AVHRR data is 1.1 km at nadir. However, in GAC data, four out of every five samples along the scan line are used to calculate one average value, and the data from only every third scan line are taken. As a result, the spatial resolution of GAC data near the subsatellite point is actually 1.1 by 4 km resolution with a 3 km gap between pixels across the scan line, although generally treated as 4 km resolution. Revised postlaunch calibration constants that correct for the degradation of the AVHRR channel 1 sensor are used to convert the AVHRR digital counts to reflectance [*Rao and Chen*, 1999]. As discussed in the previous section, to minimize the effect of specular reflection from the ocean surface, only the antisolar side of the scan line with viewing angle >40° away from the specular ray has been included in the analysis. Reflectance of radiation at ocean surface at each pixel is based on surface wind speeds obtained from NCEP/NCAR reanalysis (2.5° horizontal resolution) corresponding to each day.

Pixels that are filled partially or fully by clouds are detected and rejected using three tests: (1) the threshold method (brightness temperatures in channels 4 and 5), (2) the spatial

coherence test (brightness temperatures in channels 4 and 5) [*Coakley and Bretherton*, 1982], and (3) the visible and near-IR channel ratio method [*Durkee et al*., 1991]. In the threshold method all pixels having channel 4 and 5 brightness temperatures of <283 K are identified as cloudy. The value of 283 K was arrived at after considering histograms of brightness temperature during the period of observation and is sufficiently below the sea surface temperature (SST) at 25°S, which is the coldest region in the data used. The threshold method detects pixels filled by medium and high clouds. Partially filled pixels with nonuniform clouds are detected by a spatial coherence test applied to both channels 4 and 5, where brightness temperatures of the middle pixel of a 3 × 3 array are compared with the adjacent pixels. All the pixels must fall within 1 K of each other for the pixel to be classified as clear. Clear pixels adjacent to cloudy pixels also are rejected to avoid any possible contamination from cloud reflected radiation reaching the sensor. Both the above methods are less efficient in identifying low-level homogeneous clouds. They are identified on the basis of the weak spectral dependence of scattering by clouds. If the channel 2/channel 1 albedo ratio is >0.8, the pixel is identified as cloudy [*Durkee et al*., 1991]. Data within 0.2° of continental areas are discarded to avoid reflection effect from land areas.

AOD at the pixel is determined by comparing the observed reflectance with the look-up table. Since the look-up table is at discrete intervals of solar and satellite positions, wind velocities, and aerosol optical depth, the AOD at any intermediate value is determined by linearly interpolating between these intervals. The in situ measured single scattering albedo at Kaashidhoo was ~0.9 at surface. However, aerosols of purely oceanic origin do not have significant absorption and have a single scattering albedo of ~1.0. Background AOD due to aerosols of ocean origin is small (~0.05). Thus the application of the absorbing aerosol model over the whole area and all optical depths may not be valid. Here we have separately retrieved AOD using the absorbing model described in section 2.1 (with $\omega = 0.9$ at the surface) and $\omega = 1.0$ and combined the AOD retrieved using these two models in the following way to account for this nonabsorbing component. If AOD retrieved using $\omega = 1.0$ at a pixel is ≤0.05, this is taken as the actual AOD at the pixel. When AOD retrieved using the absorbing model at a pixel is >0.15, this value is taken as the AOD at the pixel. For values of AOD between 0.05 and 0.15 the AOD at the pixel is obtained by interpolating between the retrieved AOD using the absorbing model and that obtained using $\omega = 1.0$, after assuming a nonabsorbing AOD of 0.05. Thus for higher AOD the value will be closer to that obtained using the absorbing model. This accounts for the nonabsorbing background aerosols of marine origin ($\omega = 1.0$) and continental aerosols that are observed to have single scattering albedos of ~0.9 at the surface.

3. Validation: Comparison of the Retrieved AOD With in Situ Measurements

Spectral aerosol optical depth measurements at seven wavelengths (340, 380, 440, 500, 670, 870, and 1020 nm) were made at Kaashidhoo using the automatic CIMEL Sun/sky radiometer, which is part of the Aerosol Robotic Network (AERONET) [*Holben et al*., 1998]. Measurements of spectral AOD were also made using a spectroradiometer onboard the Indian R/V *Sagar Kanya* during its cruise period from February 18 to March 28, 1998, between 20°N and 20°S in the Indian Ocean

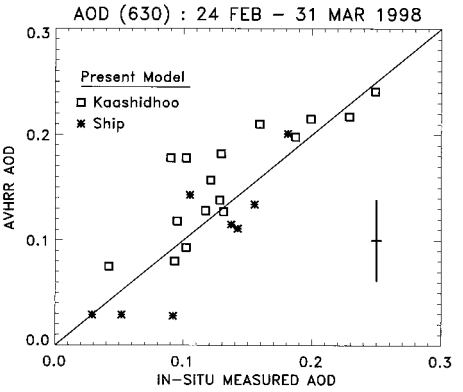

Figure 2a. Comparison between the satellite-derived aerosol optical depth (AOD) using the present model and the colocated in situ measured AOD. See text for details.

[*Meywerk and Ramanathan*, 1999]. For comparison of satellite-retrieved AOD with the Kaashidhoo data we consider AVHRR data within ±0.1° but outside ±0.15° latitude and longitude (to avoid the influence of land reflection from the very tiny island of ~1 km horizontal extent) and within a time interval of ±60 min. For comparison with ship-borne measurements, AVHRR data within ±2° latitude and longitude and within a time interval of ±60 min is considered. Figure 2a shows the intercomparison between in situ measurements and AVHRR-retrieved AOD. The slope of the variation is 0.94, and the offset is 0.018. The rms deviation between the two measurements is 0.036, and the correlation coefficient is 0.84. Both the measurements are within ±0.03 in most of the cases, and the maximum deviation observed is ±0.08.

Figure 2b shows a comparison of in situ measurements with the AVHRR data analyzed using a single scattering albedo of 1.0 (nonabsorbing aerosols). In this case the AVHRR-retrieved AOD is underestimating the actual AOD. The difference between the in situ and AVHRR-derived AOD is high at higher optical depths. The slope of the variation is 0.68, and the offset is 0.025. The maximum difference between Figures 2a and 2b is observed at higher values of AOD. A comparison of slopes of the variations in Figures 2a and 2b (in addition to the in situ data) also suggests that the actual aerosol single scattering albedo is closer to that assumed in the absorbing aerosol model, as may be seen from the following discussion.

For illustration of the physical processes involved we may

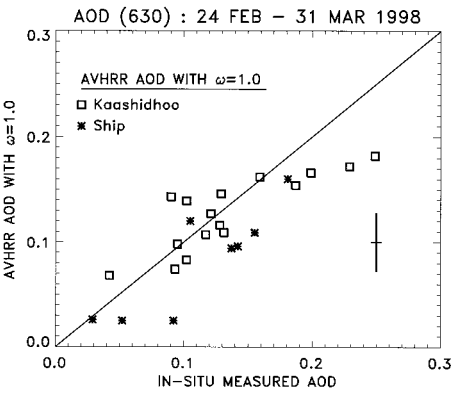

Figure 2b. Same as Figure 2a but for satellite-derived AOD based on conservative scattering ($\omega = 1.0$).

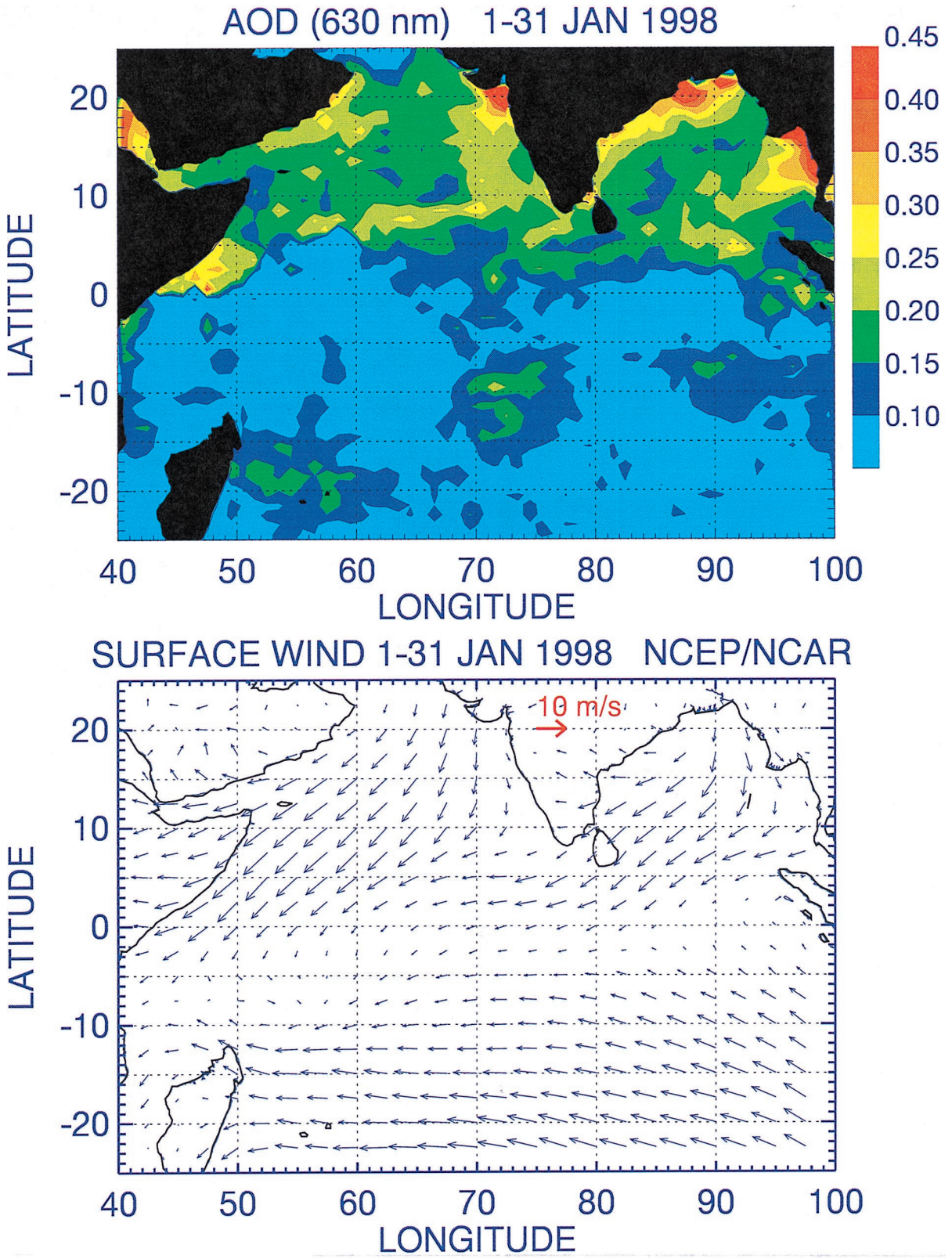

Plate 1. (top) Map of the monthly mean satellite-derived AOD during January 1998 and (bottom) prevailing monthly mean atmospheric circulation at surface during January 1998 based on National Centers for Environmental Prediction (NCEP)/National Center for Atmospheric Research (NCAR) reanalysis.

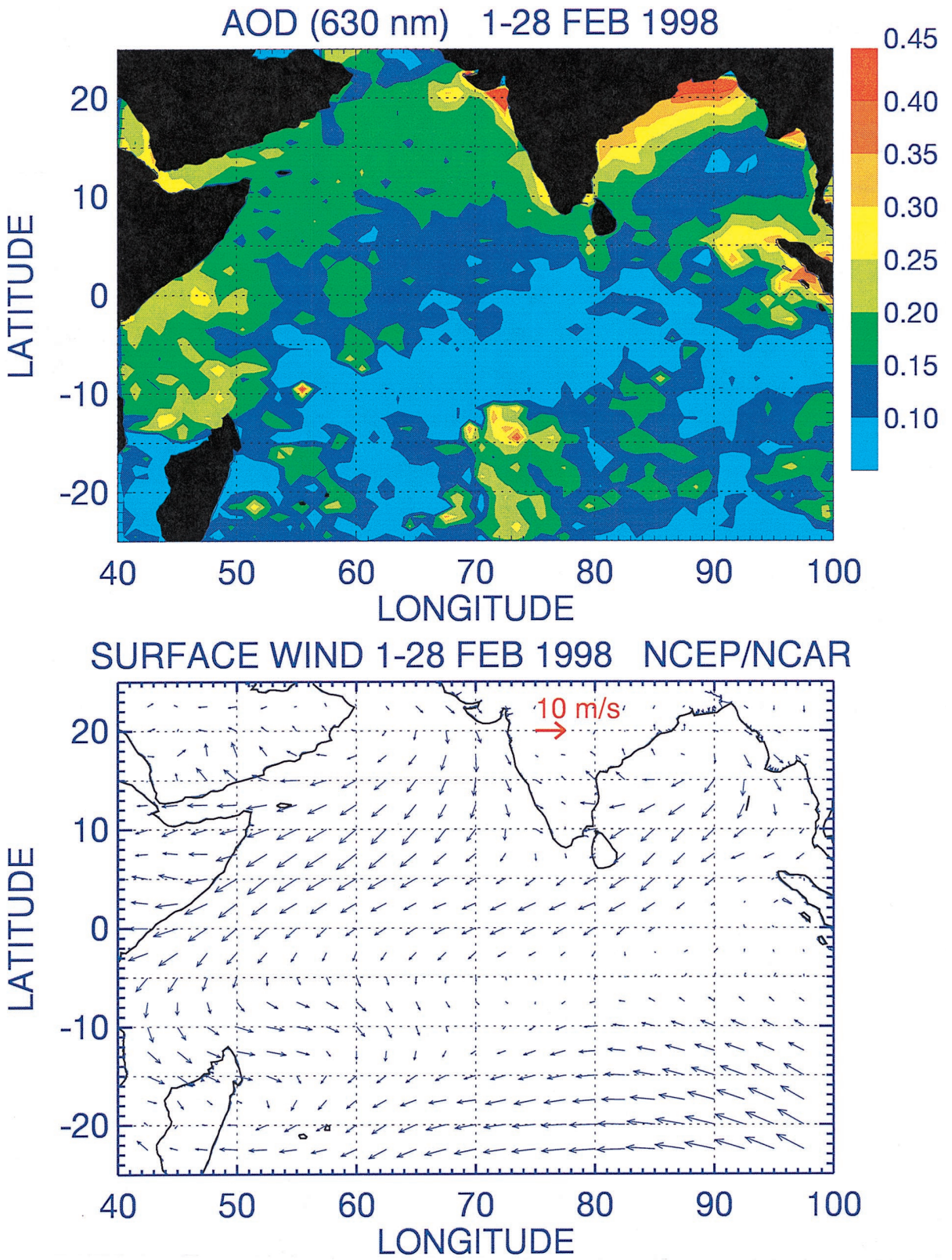

Plate 2. Same as Plate 1 but for February 1998.

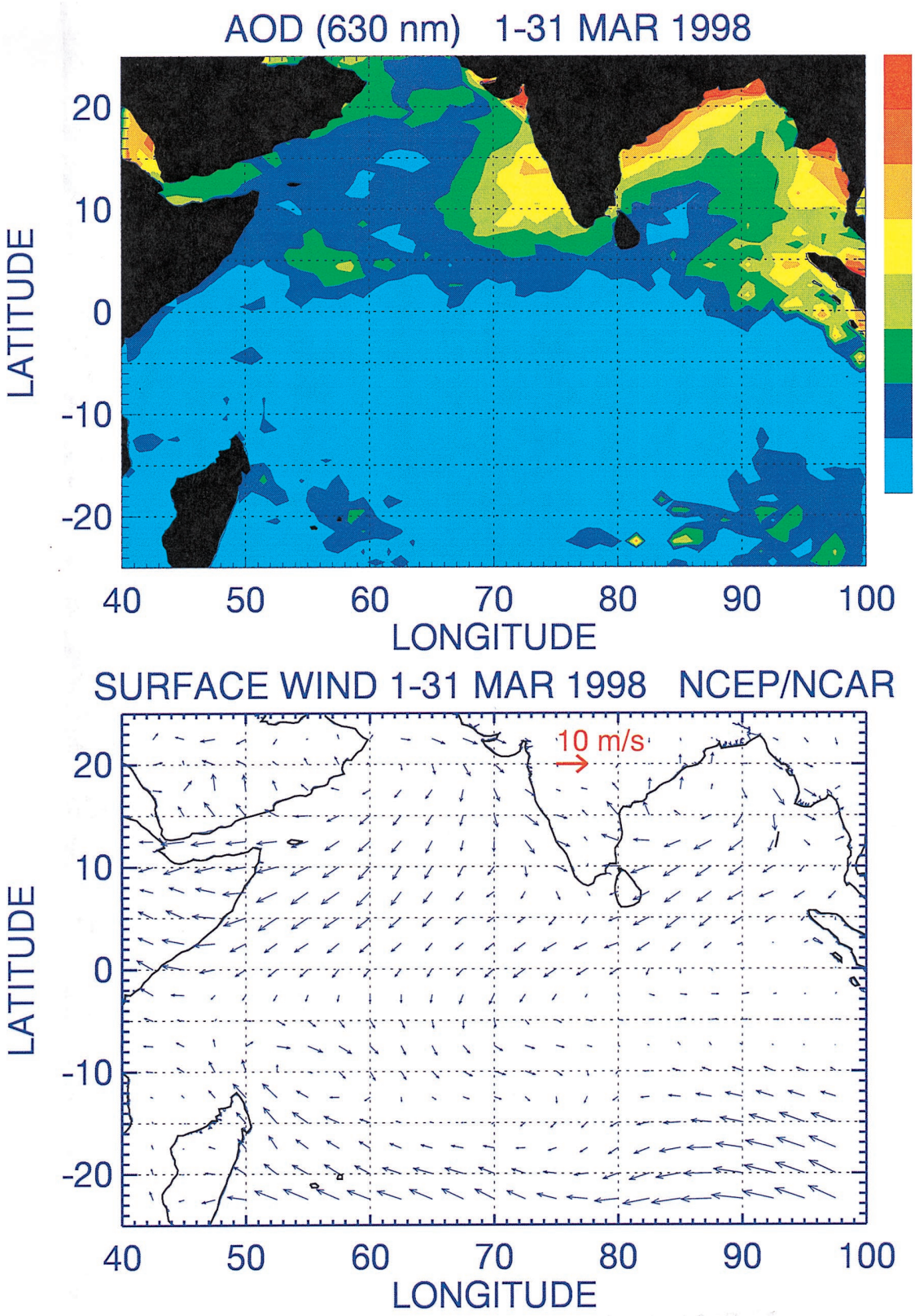

Plate 3. Same as Plate 1 but for March 1998.

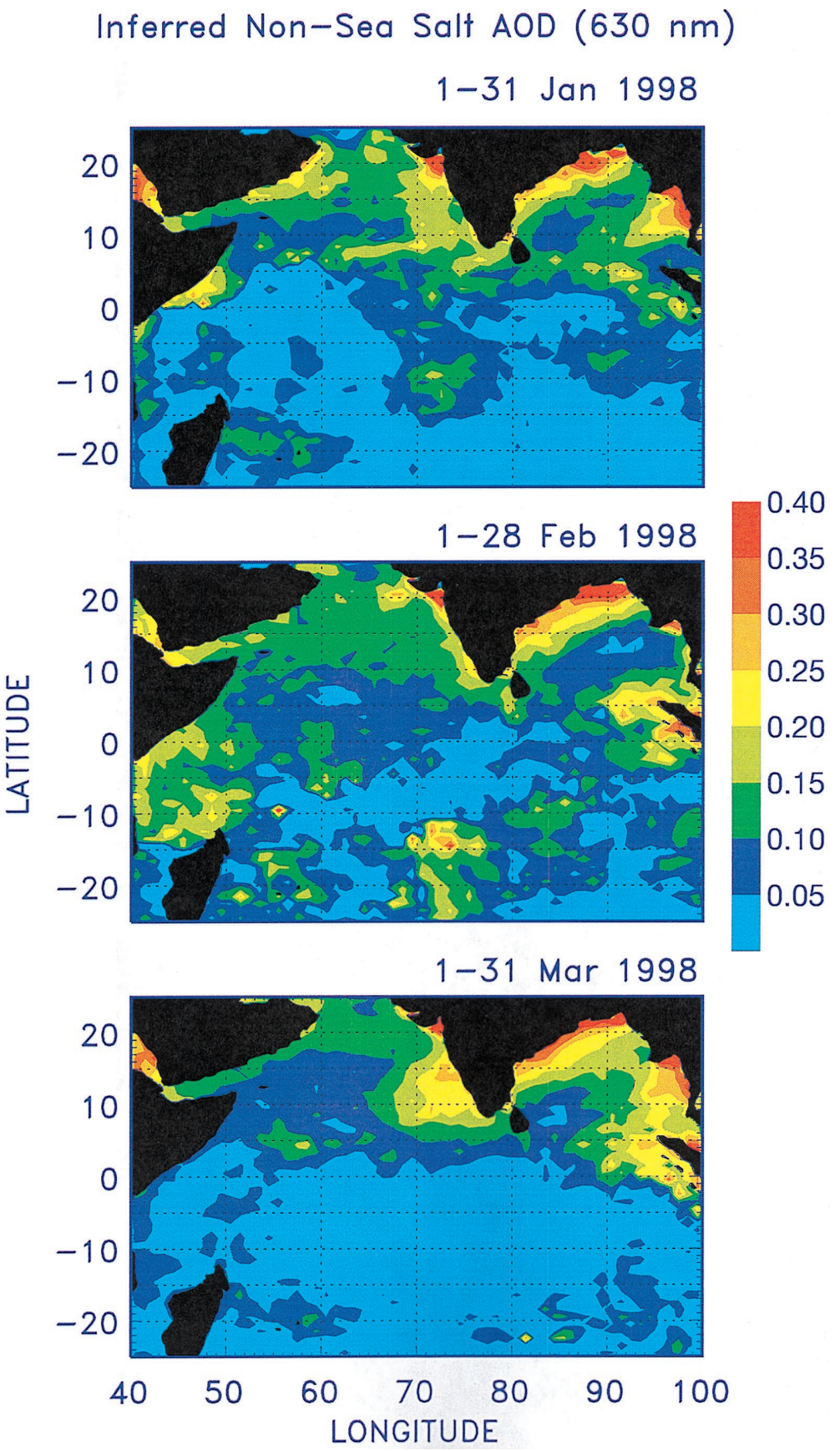

Plate 4. Maps of the inferred monthly mean non-sea-salt component of AOD during January, February, and March 1998 obtained by subtracting the estimated sea salt component from the total AOD.

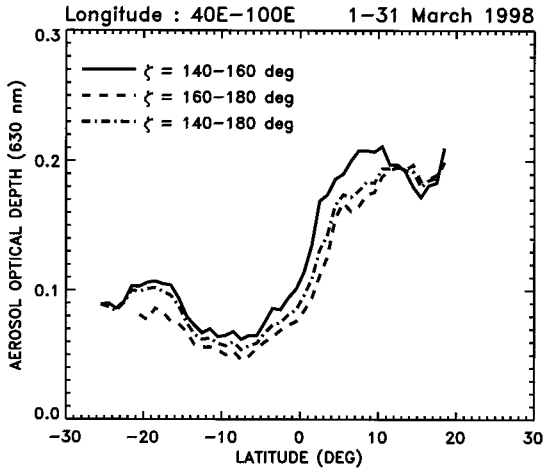

Figure 3. Latitudinal variation of monthly mean AOD during March 1998 in the longitude sector 40°–100°E derived from backscattering angles ζ between 140°–160° (solid line) and 160°–180° (dashed line).

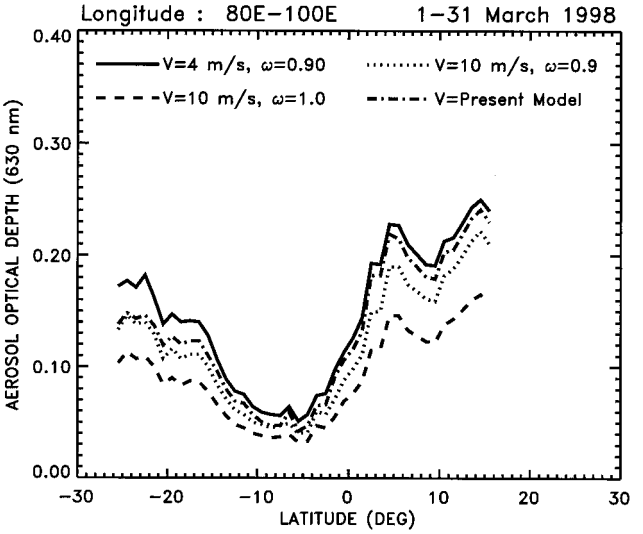

Figure 4. Latitudinal variation of monthly mean AOD during March 1998 in the longitude sector 80°–100°E for the absorbing aerosol model ($\omega = 0.9$ at surface) with wind speeds of 4 (solid line) and 10 m s^{-1} (dotted line) and the nonabsorbing model ($\omega = 1.0$) with wind speed equal to 10 m s^{-1} (dashed line).

consider radiance reaching the satellite sensor because of scattering by aerosols, $\rho_a(\theta, \theta_0, \phi)$, above a dark object in the single scattering approximation given by

$$\rho_a(\theta, \theta_0, \phi) = \omega\tau_a P(\theta, \theta_0, \phi)/(4\mu\mu_0), \quad (1)$$

where θ is satellite zenith angle, θ_0 is solar zenith angle, ϕ is azimuth of scattered radiation from the solar beam, $\mu = \cos(\theta)$, $\mu_0 = \cos(\theta_0)$, ω is aerosol single scattering albedo, τ_a is aerosol optical depth, and $P(\theta, \theta_0, \phi)$ is aerosol scattering phase function.

From (1), for a given aerosol optical depth, radiance reaching the satellite sensor because of scattering by aerosols depends on the product of the phase function and the single scattering albedo. Thus slope of the variation between the actual and satellite-retrieved AOD will also be proportional to the product of single scattering albedo and the phase function. In principle, the slope will be unity when assumed values of $\omega P(\theta, \theta_0, \phi)$ match with actual values. The effect of a weakly reflecting surface like ocean instead of a dark object is primarily to produce a shift in the value of retrieved AOD and to affect the slope to a lesser extent. Note that we have used the phase function based on observations, and thus the controlling parameter that determines the slope of the variation between observed and satellite-retrieved AOD in the present case is the aerosol single scattering albedo.

The aerosol model used in the present study is based on the data at one site in the Indian Ocean, and the effect of using the scattering phase function based on this model for the whole region of study is discussed below. For this we have separated the AOD into two sets depending on the backscattering angle of the solar radiation scattered into the direction of the satellite sensor: (1) between 140° and 160° and (2) between 160° and 180°. The scattering angle of backscattered radiation reaching the satellite sensor and the corresponding aerosol scattering phase function depend on the satellite zenith angle, the solar zenith angle, and the relative azimuth between the Sun and the satellite. Any significant difference in the angular variation of aerosol phase function will cause the AOD obtained from the two sets to differ, with a nearly constant difference. Figure 3 shows the monthly mean latitudinal variation of AOD during March 1998 for these two ranges of backscattering angle (see section 4 for details) in the longitude band of 40°–100°E. Close agreement between the two curves with only a small systematic difference indicates that the phase function used in the present analysis is mostly valid in the whole region of study. Small differences between the two curves are partly due day-to-day and spatial variability of AOD since on any given day, the two sets of satellite zenith angles represent two separate regions and during the 1 month period all regions are covered several times in the two ranges of satellite zenith angles to produce the monthly average.

To assess the dependence of the AOD on wind speed and single scattering albedo, the data were analyzed using different combinations of single scattering albedo and wind speeds. Figure 4 shows the latitudinal variations of average AODs in the longitude region of 80°–100°E (see section 4 for details) during March 1998 obtained by analyzing the AVHRR data with (1) the absorbing model ($\omega = 0.9$ at surface) and $V = 4.0$ m s^{-1}, (2) the absorbing model ($\omega = 0.9$ at surface) and $V = 10.0$ m s^{-1}, and (3) the nonabsorbing model ($\omega = 1.0$ at surface) and $V = 10$ m s^{-1}. The difference between curves for cases 1 and 2 shows the sensitivity in the AOD due to changes in surface reflectance caused by wind speed, and the difference between cases 2 and 3 indicates the sensitivity due to single scattering albedo. Comparison between cases 1 and 2 suggests that the effect of wind speed is mainly to produce a nearly constant shift in the retrieved AOD. Comparison of cases 2 and 3 shows that variation due to single scattering albedo is very small at low AOD (~0.05) and increases with increasing AOD (~0.03 at AOD of 0.20). Latitudinal variation of AOD when the AVHRR data are analyzed using the present method (which accounts for the actual wind speed) is also shown in Figure 4 for comparison. Note that this curve is close to case 1 (absorbing model and $V = 4.0$ m s^{-1}) at most of the latitudes. The deviation between the two is high south of ~17°S, where the wind speed is higher. In this region the AOD determined using

the present method is closer to case 2 (absorbing model and $V = 10$ m s^{-1}).

4. Results

4.1. Regional Distribution of AOD

Plates 1, 2, and 3 show spatial distributions of monthly average satellite-derived aerosol optical depth at the wavelength 630 ± 50 nm during January, February, and March 1998, respectively. Note that the AODs were calculated for each pixel of 1.1 × 4 km resolution, which were then spatially and temporally averaged to a latitude and longitude bin of 1° resolution. The AOD is significantly higher in the Northern Hemisphere compared to the Southern Hemisphere during all 3 months, with the highest values of AOD near the continents. Plumes of aerosols originating from Arabia, the Indian subcontinent, and southeast Asia extending up to deep ocean areas are observed in the Northern Hemisphere. In the Southern Hemisphere, the highest AOD is observed during February when the AOD is only slightly smaller than that in the Northern Hemisphere.

4.1.1. Arabian Sea. In January the AOD is >0.18 over most of the Arabian Sea, with the highest values of AOD of ~0.30 close to Arabia and the west coast of India. During this time the spatial gradient of AOD close to coastal India is higher than that from Arabia. Plate 1 also shows an aerosol plume off the Arabian coast that extends to ~1000 km away from the coast. In general, the AOD is highest in January compared to February and March over the whole Arabian Sea. The aerosol plume present in January off Arabia is still present in February, albeit with decreased intensity. In February another aerosol plume is observed farther to the west. It is interesting to note that this plume extends from the Horn of Africa to ~15°S with decreasing AOD toward the south. In March, the AOD is less than those during January and February over the central and western Arabian Sea. However, the aerosol plume appearing off the southwest coast of India intensifies with an AOD of 0.30 near the coast, which decreases to <0.15 over a distance of ~1500 km away from the coast.

4.1.2. Bay of Bengal. Generally, the AOD in the Bay of Bengal is comparable to that of the Arabian Sea, with high values during January. However, the coastal values are higher than those in the Arabian Sea, with values of AOD exceeding 0.4. This region of high AOD is associated with a large spatial gradient, with AOD rapidly decreasing away from the coast. Another prominent region of high AOD in the Bay of Bengal is close to southeast Asia. A strong aerosol plume with an AOD comparable to that observed in north Bay of Bengal is observed off Sumatra during February and March. The spatial gradient of the AOD in this aerosol plume is smaller than that observed off the Indian coast. The AOD and the horizontal extent of this plume are higher during March compared to February. This plume is not noticeable in January. A high AOD is also observed close to southern parts of Myanmar and Thailand and is present during all 3 months with varying aerosol abundance. A region of minimum AOD is observed at central parts of the Bay of Bengal during all 3 months, which is sandwiched between the areas of high AOD at the northwest coast of India and southeast Asia.

4.1.3. Tropical Indian Ocean. Northern parts of the Indian Ocean bordered with the Arabian Sea and the Bay of Bengal are characterized by a large decrease in AOD from its northern boundary up to around the equator. A large pool of low AOD is observed south of the equator with a horizontal extent that varies from month to month. The latitudinal range of this low-AOD area (with AOD <0.1) is at a maximum in March (~20°) and a minimum in February (~10°). The spatial distribution of aerosols in February is characteristically different from those during January and March both in the northern and southern parts of the Indian Ocean. The AOD in the Southern Hemisphere Indian Ocean is highest in February with an aerosol plume west of 50°E off the Somalia coast extending up to south of 15°S close to Madagascar with diminishing aerosol optical depth from north to south.

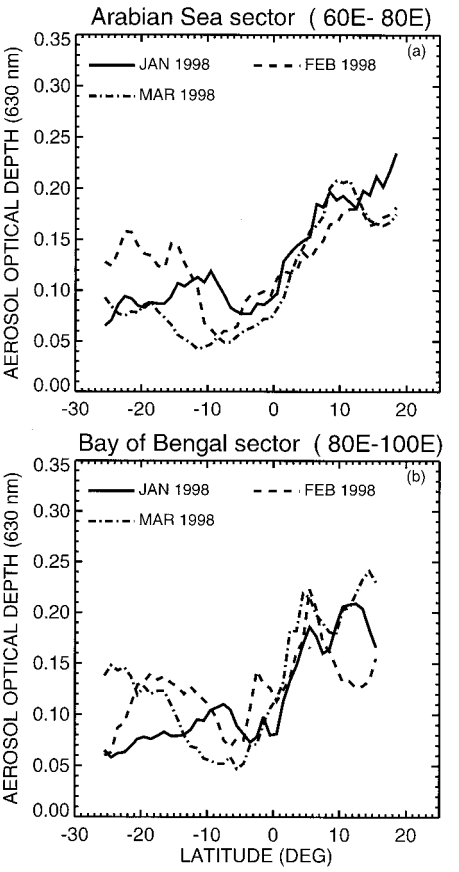

Figure 5. Latitudinal variation of AOD during January, February, and March 1998 for two longitude regions: (a) 60°–80°E (Arabian Sea-Indian Ocean sector) and (b) 80°–100°E (Bay of Bengal-Indian Ocean sector).

4.2. Latitudinal Variation of AOD

The latitudinal variation of AOD in the Arabian Sea, Bay of Bengal, and Indian Ocean during each month is obtained by separately averaging all the AOD values in the longitude ranges 60°–80°E (Arabian Sea-Indian Ocean sector) and 80°–100°E (Bay of Bengal-Indian Ocean sector) during the corresponding month. Figures 5a and 5b show the latitudinal variation of AOD in the 60°–80°E and 80°–100°E longitude sectors, respectively.

The general features revealed by Figures 5a and 5b are as follows: (1) There is significant month-to-month variability; (2) the southward migration of the AOD minima from January to March closely follows the migration of the ITCZ; (3) the AOD in the Northern Hemisphere is larger than that in the Southern Hemisphere by ~50–100%; and (4) The secondary maxima

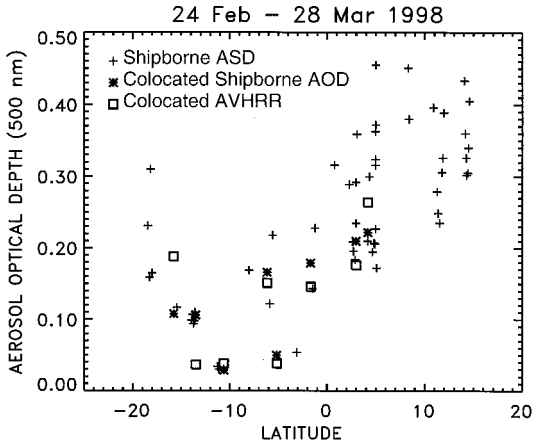

Figure 6. Latitudinal variation of the daytime shipborne measurements of AOD during February 24 to March 28, 1998. Asterisks indicate the shipborne measurements colocated with advanced very high resolution radiometer (AVHRR) data. Also shown are the colocated satellite-derived AODs for comparison.

around 20°S is clearly seen in the zonal average. These patterns derived from satellite data are also confirmed by shipborne data (Figure 6) especially the primary and secondary maxima respectively in the 10°–20°N and 15°–20°S regions.

Figure 6 shows latitudinal variation of the AOD at 500 nm in the longitude range of 57°–73°E observed from *Sagar Kanya* during its cruise period between February 18 and March 28, 1998. The cruise track was in the north-south direction close to 70°E ± 3° between 15°N and the equator. South of the equator, it had a southwestward tilt in the track and was between 0N, 70°E ± 3° and 20°S, 57°E. The ship was in its southernmost position on March 13. All the observations made using the spectroradiometer are shown in Figure 6, and the relatively large spread in AOD for a given latitude is due to the short period variations during the daytime. Shipborne AOD values colocated (in space and time) with AVHRR are shown with a different symbol for comparison with the corresponding satellite-retrieved AOD values. The satellite-retrieved AOD at 630 nm is converted to 500 nm on the basis of Mie calculations for the assumed aerosol properties used to retrieve AOD from the satellite data. Figure 6 reveals a large latitudinal gradient in AOD south of ~10°N, reaching a minimum value at ~10°S. The AOD increases rather slowly south of 10°S up to 18°S.

4.3. Spatial Distribution of Non-sea-salt AOD

The contribution of the non-sea-salt component of AOD (τ_{NSS}) was inferred by subtracting the estimated wind-dependent sea salt component (τ_{SS}) from the total AOD. The sea salt component was estimated using the exponential relationship between wind speed (U in m s^{-1}) and τ_{SS} given by

$$\tau_{SS} = \tau_{SS0} e^{(0.16U)}, \quad (2)$$

where τ_{SS0} is the aerosol optical depth due to sea salt alone at $U = 0$ m s^{-1} [*Erickson et al.*, 1986; *Krishna Moorthy et al.*, 1997]. This model represents the aerosol loading in the atmosphere due to increased wind speed and has been found to be in reasonably good agreement with observations [*Tegen et al.*, 1997]. We have taken τ_{SS0} as 0.02, which is the minimum aerosol optical depth at 630 nm observed over the whole study area using both satellite-based and shipborne measurements.

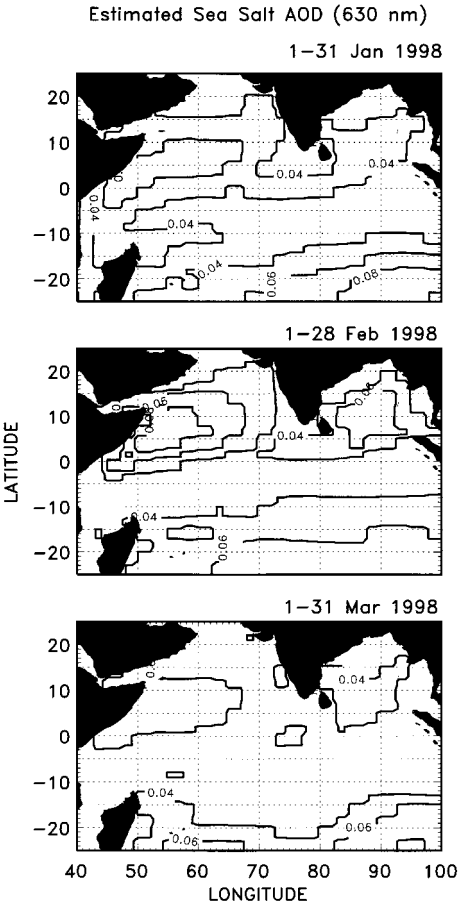

Figure 7. Contour maps of sea salt component of AOD during January, February, and March 1998 estimated on the basis of monthly mean wind speed.

At Kaashidhoo the τ_{SS} estimated on the basis of the above model and the actual wind speed are in the range 0.03–0.06, which is in good agreement with the in situ observed sea salt AOD [*Satheesh et al.*, 1999].

Figure 7 shows the contour maps of τ_{SS} estimated for each month on the basis of the above model for the monthly mean surface wind speeds shown in Plates 1–3. The τ_{SS} is found to have high values during January and February in the southeast and northwest Indian Ocean region with a maximum value of ~0.10. Plate 4 shows the spatial distribution of the non-sea-salt component of AOD during the 3 months obtained by subtracting τ_{SS} from the respective monthly mean AOD (Plates 1–3). Plate 4 confirms our earlier deduction that the high concentration of aerosols observed in the total AOD (seen as the plume-like structures close to continents in Northern Hemisphere) is mainly due to the non-sea-salt components. Values of τ_{NSS} exceed 0.15 over most of the Northern Hemisphere oceans during January and are >0.10 over during February and March. Further, in the Southern Hemisphere, τ_{NSS} exceeds 0.10 over a large the area and is significantly larger than τ_{SS}, particularly during January and February. These high values of τ_{NSS} appear to be closely linked to the aerosol plumes originating in the Northern Hemisphere, which extend up to deep Southern Hemispheric ocean areas. This link is clearly seen in the equatorial Indian Ocean over the western parts near the Horn of Africa and in the eastern parts close to

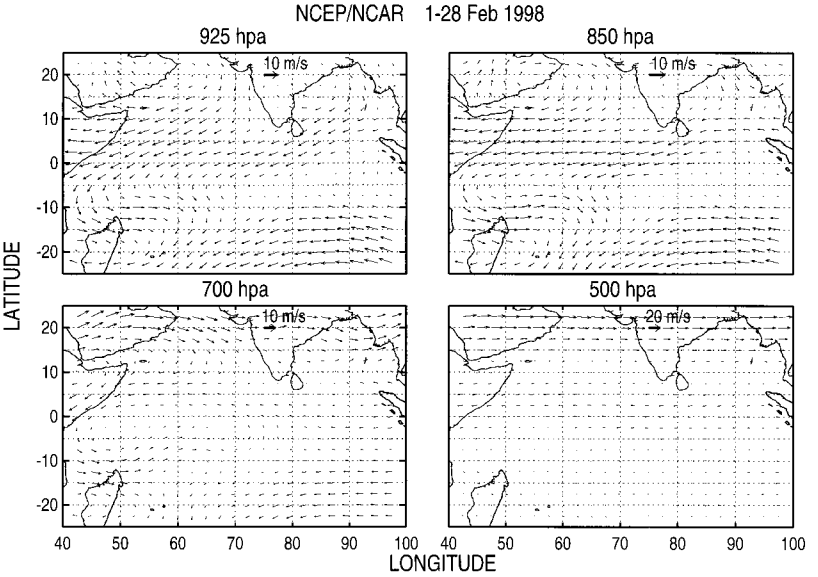

Figure 8. Prevailing monthly mean atmospheric circulation during February 1998 at 925, 850, 700, and 500 hpa based on the NCEP/NCAR reanalysis.

Sumatra and Indonesia. These findings regarding τ_{NSS} need to be confirmed with in situ data.

5. Role of Transport in the Observed Regional Aerosol Distribution

Atmospheric circulation and aerosol lifetime are the dominating factors controlling the spatial distribution and transport of aerosols from the continent to the ocean areas. The northeast monsoon (December–March) is primarily driven by differential heating between land areas in the Indian subcontinent and the adjacent ocean areas. The large high-pressure system that forms over central India gives rise to the Indian dry season and generates a persistent northeasterly offshore flow [*Krishnamurti et al*., 1998]. Figure 8 shows the atmospheric circulation obtained from NCEP/NCAR reanalysis at 925, 850, 700, and 500 hpa levels during February 1998. Surface winds for each month are shown in Plates 1–3. Comparison of the maps of AOD with atmospheric circulation clearly reveals the transport of aerosols from the continental areas into the otherwise pristine oceans. Atmospheric circulation and trajectory analysis during February 15 to March 31, 1998, over the INDOEX region were carried out by *Jha and Krishnamurti* [1998], which showed that air parcels originating in the lower troposphere and midtroposphere over continental areas reach thousands of kilometers into deep ocean areas in <10 days because of the prevailing northeasterly winds. An association between the observed spatial distribution of aerosols and the prevailing atmospheric circulation for different ocean areas is discussed below.

5.1. Arabian Sea

The regional maps of AOD and the prevailing atmospheric circulation reveals that the transport of aerosols occurs from two source regions: Arabia and the Indian subcontinent. The anticyclonic circulation with its center at ~20°N, 60°E causes northwesterly winds over Arabia between the surface and 700 hpa level. Close correlation between the northwesterly offshore flow from Arabia and the non-sea-salt aerosol plumes off the Arabian coast demonstrates the transport of aerosols from Arabia (which could be predominantly mineral dust) into the ocean areas [also see *Krishnamurti et al*., 1998]. Penetration of this plume to regions of the ocean far from the coast is aided by the prevailing high wind speed observed over the Arabian Sea. For example, a high concentration of mineral dust was observed at Kaashidhoo Island in the Indian Ocean during the same observation period (Satheesh et al., submitted manuscript, 1999). The large concentration of mineral dust over the Indian Ocean was also noted by earlier studies [*Pordi et al*., 1983; *Savoie et al*., 1987].

On the other hand, northeasterlies transport aerosols from the Indian subcontinent into the Arabian Sea. The offshore component of wind is large at the lower tropospheric levels over the Indian subcontinent, particularly at the southwest (SW) coast of India. The trajectory analysis by *Jha and Krishnamurti* [1998] has also shown large southwestward transport of air from peninsular India at the lower tropospheric levels, with an air mass transit period of about a week between the SW coast of India and the equator. These transports cause the large values of AOD off the west coast of India. The large aerosol plume off the southwest coast of India during March (Plate 3) is particularly notable.

5.2. Bay of Bengal

Transport of aerosols into the Bay of Bengal occurs from the Indian subcontinent and southeast Asia. The anticyclonic circulation over the northwest Bay of Bengal, which extends from the surface up to ~750 hpa level (Figure 8), causes considerable offshore transport of air from India (the Bengal region) to the northern Bay of Bengal. The high aerosol optical depth observed close to India during all 3 months over northern Bay of Bengal is associated with this offshore flow. The height of aerosol transport in this region appears to be between surface and 750 hpa level. Trajectory analysis by *Jha and Krishnamurti* [1998] showed the transport of air from eastern parts of India reaching the Bay of Bengal in <5 days at 990 and 850 hpa levels. However, this offshore flow does not penetrate deep in

to the Bay of Bengal, which results in the large spatial gradient in AOD observed in the northwest Bay of Bengal.

Considerable transport of air from southeast Asia (Thailand, Sumatra, and Indonesia) to the Bay of Bengal occurs between the surface and 850 hpa through the easterly and northeasterly winds in this region. The AOD over the Bay of Bengal close to Thailand and Sumatra is as high as that at the north Bay of Bengal, particularly during February and March. The surface wind flow is easterly over Thailand but rather weak close to Sumatra because of its proximity to the ITCZ. However, lower tropospheric flow is easterly south of 10°N, and this could enhance the transport of aerosols from Sumatra and Indonesia into the Bay of Bengal. Aerosol abundance in the Bay of Bengal off Sumatra is higher in March compared to February and is absent in January. This has obviously resulted from the westward transport of aerosols arising from significant forest fires at Indonesia and north Sumatra, which occurred from the end of January until the middle of May [*Schweithelm*, 1998]. The earth probe Total Ozone Mapping Spectrometer (TOMS) also detected Indonesian forest fires during this period. *Husar et al*. [1997] showed that there is considerably large southward transport of aerosols from eastern parts of China to near the equator during December to May. This will also enhance the aerosol concentration in the region around Indonesia and Sumatra, which could be finally transported to the Bay of Bengal.

5.3. Tropical Indian Ocean

The AOD is <0.1 at the equatorial Indian Ocean, which is also the location of the ITCZ. The region of minimum AOD shows a southwestward tilt similar to that seen in the location of the ITCZ. It is important, though, to note that ITCZ is the maximum cloudy area and the retrieval of AOD is possible only during clear-sky conditions. However, the in situ measurements also show such low AOD, which is in very good agreement with the satellite-derived AOD (Figure 6). The aerosol removal mechanism in the ITCZ is very efficient through aerosol washout and rainout, which result in shorter residence times of aerosols and low aerosol loading. The large latitudinal gradient of AOD observed at the northern boundary of the Indian Ocean is most likely due to this reduction in aerosol lifetime.

In the Southern Hemisphere Indian Ocean the wind is strongly easterly to southeasterly between the surface and 700 hpa level in the 15°–30°S latitude band. The high surface wind speed produces higher amount of sea salt in this region (Figure 7). However, the non-sea-salt component of AOD (Plate 4) exceeds the sea salt component in the Southern Hemisphere Indian Ocean. Considerable amounts of the non-sea-salt aerosols appear to arise from the interhemispheric transport from the polluted Northern Hemisphere. The progressively increasing residence time of aerosols toward the south of the ITCZ due to decreasing precipitation can lead to the accumulation of aerosols that had penetrated into the Southern Hemisphere through the ITCZ. The 10 day back trajectories by *Jha and Krishnamurti* [1998] during February 20 to March 2, 1998, have shown subsidence of air at 20°S, 60°E at the 850 hpa level, which was originated at 750 hpa in the Arabian Sea and close to the Somalia coast. The transport of Northern Hemisphere aerosol-laden air also occurs at the central and east equatorial Indian Ocean because of the southwestward tilt of the ITCZ [*Krishnamurti et al*., 1998]. Aerosols penetrating to the eastern equatorial Indian Ocean will be carried westward by the prevailing strong easterly winds south of the ITCZ. This is more evident in January and February (Plate 4) when the high concentration of non-sea-salt aerosols in the Southern Hemisphere appears to be closely linked to the aerosol plume arising from east Asia, including Indonesia and Sumatra.

Tegen and Miller [1998] estimated that significant transport of Australian dust into the eastern parts of Indian Ocean can occur during December–February. The dust transport from Australia due to the prevailing high southeasterly wind also could have contributed to the high non-sea-salt AOD observed in eastern parts of the Indian Ocean. Aerosols from southern Africa could also reach the Indian Ocean through the middle and upper troposphere south of 25°S, where the wind is predominantly westerly during the period of observation. However, aerosol production in Southern Hemisphere Africa due to biomass burning during January–March is considerably less [*Cahoon et al*., 1992]. Another source of the high concentration of aerosols observed in the Southern Hemisphere could be oceanic sources of non-sea-salt (nss) sulfate. However, high-nss sulfate is not seen in the Indian Ocean around 20°S during January–March in most of the models [e.g., *Chin et al*., 1996]. In short, a combination of interhemispheric aerosol transport through the western and eastern parts of the tropical Indian Ocean, an increase in aerosol lifetime south of the ITCZ, increased sea salt production due to higher wind speed, and transport of Australian dust appears to have caused the maximum AOD observed at $\sim$20°S.

6. Conclusions

In this study, aerosol optical depth is retrieved from the AVHRR data over Arabian Sea, Bay of Bengal, and Indian Ocean during January, February, and March (northeast monsoon season). The retrieval is based on the aerosol scattering and absorption properties measured at Kaashidhoo Island (4.96°N, 73.46°E), which is centrally located in the study area. Multiple scattering and absorption by aerosols and molecules and the variability in sea surface reflectance due to daily variation in wind speed are accounted for in the aerosol retrieval. Spatial distribution of AOD and its comparison with prevailing atmospheric circulation shows the following features.

1. Transport of continental aerosols originating at three different source regions, namely, Arabia, the Indian subcontinent, and southeast Asia, which penetrate deep into the ocean areas mainly between the surface and the midtroposphere are clearly observed in the Northern Hemisphere. The non-sea-salt component of AOD is more than 3 times that of the sea salt over most of the ocean areas. Transport of aerosols by northwesterly winds from Arabia and northeasterly winds from the Indian subcontinent are the major sources of high concentration of aerosols in Arabian Sea. In the Bay of Bengal the AOD is comparable to that over the Arabian Sea and has its origin from India and southeast Asia, including Indonesia and Sumatra. An intense aerosol plume is observed off Sumatra during February and March and is highly correlated with the forest fires in Indonesia and Sumatra during that time.

2. Minimum AOD is observed in the ITCZ region, which is located between the equator and 10°S during the observation period. The southwestward tilt of the ITCZ west of 80°E is also observed in the location of minimum AOD. Low AOD in the ITCZ region is mainly due to shorter aerosol residence times because of the highly efficient aerosol removal processes (washout and rainout) operating in this area.

3. The AOD increases with latitude in the Southern Hemisphere south of the ITCZ to reach a maximum around 20°S, particularly in February. The non-sea-salt component of AOD exceeds the sea salt component in the Southern Hemisphere, indicating the significance of other sources in addition to the wind-produced sea salt. Transport of aerosols from the Northern Hemisphere deep into the Southern Hemisphere through the western and eastern parts of equatorial Indian Ocean is observed to be an important contributor. The southwestward tilt in the ITCZ is also observed to have the potential to transport Northern Hemispheric aerosols in to the Southern Hemisphere in the central and western equatorial Indian Ocean. The high AOD observed at ~20°S appears to have been caused by the combination of interhemispheric transport of aerosols from the Northern Hemisphere, the increased aerosol lifetime south of the ITCZ, the high concentrations of sea salt aerosols, and the transport of Australian dust.

In summary, this study demonstrates that localized sources of anthropogenic aerosols, desert dust, and smoke from forest fires can influence the global oceans far removed from the sources. We point out the following major caveats on the aerosol retrieval model used in this study: (1) It is based on surface chemical measurements and atmospheric column optical data over one site (i.e., Kaashidhoo), and (2) the validation of satellite AODs used surface-based (Kaashidhoo and ship) column AODs. Hence the model needs to be verified with detailed in situ aircraft measurements. In addition, the non-sea-salt AOD is based on a model inference, which also needs verification with in situ data.

Acknowledgments. The NCEP/NCAR reanalysis is provided by the NOAA-CIRES Climate Diagnostics Center, Boulder, Colorado, from their Web site at http://www.cdc.noaa.gov. The authors thank B. Holben for providing aerosol optical depth measurements at Kaashidhoo Island in Maldives, which is part of AERONET. J. Coakley significantly improved the quality of the results presented here. This study was funded by the National Science Foundation (NSF) through grant ATM 9612887. The study was performed when one of the authors, K. Rajeev, was on leave from Space Physics Laboratory, Vikram Sarabhai Space Centre, Indian Space Research Organization, Thiruvananthapuram, India. This is Center for Clouds, Chemistry and Climate report 212 and INDOEX report 28.

References

Cahoon, D. R., B. J. Stokes, J. S. Levine, W. R. Cofer III, and K. P. O'Neil, Seasonal distribution of African savanna fires, *Nature*, *359*, 812–815, 1992.

Chester, T., A. S. Berry, and K. J. T. Murphy, The distributions of particulate atmospheric trace metals and mineral aerosols over the Indian Ocean, *Mar. Chem*., *34*, 261–290, 1991.

Chin, M., D. J. Jacob, G. M. Gardner, M. S. Foreman-Flower, and P. A. Spiro, A global three-dimensional model of tropospheric sulfate, *J. Geophys. Res*., *101*, 18,667–18,690, 1996.

Chou, M.-D., and K.-T. Lee, Parametreizations for the absorption of solar radiation by water vapour and ozone, *J. Atmos. Sci*., *53*, 1203–1208, 1996.

Coakley, J. A., and F. P. Bretherton, Cloud cover from high-resolution scanner data: Detecting and allowing for partially filled fields of view, *J. Geophys. Res*., *87*, 4917–4932, 1982.

Cox, C., and W. Munk, Measurement of the roughness of the sea surface from photographs of the sunglitter, *J. Opt. Soc. Am*., *44*, 838–850, 1954.

Durkee, P. A., F. Pfeil, E. Frost, and R. Shema, Global analysis of aerosol particle characteristics, *Atmos. Environ*., *Part A*, *25*, 2457–2471, 1991.

Erickson, D. J., J. T. Merill, and R. A. Duce, Seasonal estimates of global atmospheric sea-salt distribution, *J. Geophys. Res*., *91*, 1067–1072, 1986.

Gordon, H. R., and M. Wang, Retrieval of water-leaving radiance and aerosol optical thickness over oceans with SeaWiFS: A preliminary algorithm, *Appl. Opt*., *33*, 443–452, 1994.

Hess, M., P. Koepke, and I. Schult, Optical properties of aerosols and clouds: The software package OPAC, *Bull. Am. Meteorol. Soc*., *79*, 831–844, 1998.

Holben, B. N., et al., AERONET: A federated instrument network and data archive for aerosol characterization, *Remote Sens. Environ*., *66*, 1–16, 1998.

Husar, R. B., J. M. Prospero, and L. L. Stowe, Characterization of tropospheric aerosols over the oceans with the NOAA advanced very high resolution radiometer optical thickness operational product, *J. Geophys. Res*., *102*, 16,889–16,909, 1997.

Jayaraman, A., D. Lubin, S. Ramachandran, V. Ramanathan, E. Woodbridge, W. D. Collins, and K. S. Zalpuri, Direct observations of aerosol radiative forcing over the tropical Indian Ocean during the January–February 1996 pre-INDOEX cruise, *J. Geophys. Res*., *103*, 13,827–13,836, 1998.

Jha, B., and T. N. Krishnamurti, Real-time meteorological reanalysis atlas during pre-INDOEX Field Phase-1998, *Rep. 98-08*, *INDOEX Publ*. *20*, Dep. of Meteorol., Fla. State Univ., Tallahassee, August 1998.

Kalnay, E., et al., The NCEP/NCAR reanalysis 40-year project, *Bull. Am. Meteorol. Soc*., *77*, 437–471, 1996.

Kaufman, Y. J., D. Tanre, L. A. Remer, E. F. Vermote, A. Chu, and B. N. Holben, Operational remote sensing of tropospheric aerosol over land from EOS moderate resolution imaging spectroradiometer, *J. Geophys. Res*., *102*, 17,051–17,067, 1997.

Koepke, P., Effective reflectance of oceanic whitecaps, *Appl. Opt*., *23*, 1816–1824, 1984.

Kratz, D. P., The correlated k-distribution technique as applied to the AVHRR channels, *J. Quant. Spectrosc. Radiat. Transfer*, *53*, 501–517, 1995.

Krishna Moorthy, K., S. K. Satheesh, and B. V. Krishna Murthy, Investigation of marine aerosols over the tropical Indian Ocean, *J. Geophys. Res*., *102*, 18,827–18,842, 1997.

Krishnamurti, T. N., B. Jha, J. M. Prospero, A. Jayaraman, and V. Ramanathan, Aerosol and pollutant transport and their impact on radiative forcing over the tropical Indian Ocean during the January–February 1996 pre-INDOEX cruise, *Tellus*, *Ser. B*, *50*, 521–542, 1998.

McClatchey, R. A., R. W. Fenn, J. E. A. Selby, F. E. Volz, and J. S. Garing, Optical properties of the atmosphere, 3rd ed., *Environ. Res. Pap*. *411*, Air Force Cambridge Res. Lab., Bedford, Mass., 1972.

Meywerk, J., and V. Ramanathan, Observations of the spectral clear-sky aerosol forcing over the tropical Indian Ocean, *J. Geophys. Res*., in press, 1999.

Mishchenko, M. I., and L. D. Travis, Satellite retrieval of aerosol properties over ocean using measurements of reflected light: Effect of instrumental errors and aerosol absorption, *J. Geophys. Res*., *102*, 13,543–13,553, 1997.

Prodi, F., G. Santaciara, and F. Oliosi, Characterization of aerosols in marine environments (Mediterranean, Red Sea, and Indian Ocean), *J. Geophys. Res*., *88*, 10,957–10,968, 1983.

Ramanathan, V., et al., Indian Ocean Experiment (INDOEX) white paper, *C4 Publ. 143*, Scripps Inst. of Oceanogr., Univ. of Calif. San Diego, La Jolla, July 1995.

Ramanathan, V., et al., Indian Ocean Experiment (INDOEX): A multi-agency proposal for a field experiment in the Indian Ocean, *C4 Publ. 162*, Scripps Inst. of Oceanogr., Univ. of Calif. San Diego, La Jolla, June 1996.

Rao, C. R. N., and J. Chen, Revised post-launch calibration of the visible and near-infrared channels of the advanced very high resolution radiometer (AVHRR) on the NOAA-14 spacecraft, *Int. J. Remote Sens*., in press, 1999.

Rhoads, K. P., P. Kelley, R. R. Dickerson, T. P. Carsey, M. Farmer, D. L. Savoie, and J. M. Prospero, Composition of troposphere over the Indian Ocean during the monsoonal transition, *J. Geophys. Res*., *102*, 18,981–18,995, 1997.

Satheesh, S. K., V. Ramanathan, X. Li-Jones, J. M. Lobert, I. H. Podgorny, J. M. Prospero, B. N. Holben, and N. G. Loeb, A model for the natural and anthropogenic aerosols over the tropical Indian Ocean derived from Indian Ocean Experiment data, *J. Geophys. Res*., in press, 1999.

Savoie, D. L., J. M. Prospero, and R. T. Nees, Nitrate, non-sea-salt

sulfate, and mineral aerosol over the northwestern Indian Ocean, *J. Geophys. Res*., *92*, 933–942, 1987.

Schweithelm, J., The fire this time: An overview of Indonesia's forest fires in 1997/98, *WWF Indonesia Programme J1. Kramat Pela 3*, Gandaria Utara, Jakarta Selatan, Indonesia, May 1998.

Stamnes, K., S.-C. Tsay, W. Wiscombe, and K. Jayaweera, A numerically stable algorithm for discrete-ordinate-method radiative transfer in multiple scattering and emitting layered media, *Appl. Opt*., *27*, 2502–2509, 1988.

Stowe, L. L., A. M. Ignatov, and R. R. Singh, Development, validation, and potential enhancements to the second-generation operational aerosol product at the National Environmental Satellite, Data, and Information Service of the National Oceanic and Atmospheric Administration, *J. Geophys. Res*., *102*, 16,923–16,934, 1997.

Tanre, D., B. N. Holben, and Y. J. Kaufman, Atmospheric correction algorithm for NOAA-AVHRR products: Theory and applications, *IEEE Trans Geosci. Remote Sens*., *30*, 231–248, 1992.

Tegen, I., and R. Miller, A general circulation model study on the interannual variability of soil dust aerosol, *J. Geophys. Res*., *103*, 25,975–25,995, 1998.

Tegen, I., P. Hollrig, M. Chin, I. Fung, D. Jacob, and J. Penner, Contribution of different aerosol species to the global aerosol extinction optical thickness: Estimates and model results, *J. Geophys. Res*., *102*, 23,895–23,915, 1997.

J. Meywerk, K. Rajeev, and V. Ramanathan, Center for Clouds, Chemistry and Climate, Scripps Institution of Oceanography, University of California San Diego, 9500 Gilman Drive #0221, La Jolla, CA 92039-0221. (vramanathan@ucsd.edu)

(Received January 21, 1999; revised May 17, 1999;
accepted May 25, 1999.)